

Article

# Experimental Investigation of Impulsive Coupling Characteristics of Asteroid Simulants Based on Laser Ablation Propulsion

Yingjie Ma, Hao Chang <sup>\*</sup>, Weijing Zhou <sup>\*</sup> and Zhilong Jian

Department of Aerospace and Technology, Space Engineering University, Beijing 101416, China; mayingjie@hgd.edu.cn (Y.M.); jzl862366@163.com (Z.J.)

<sup>\*</sup> Correspondence: changhao5976911@163.com (H.C.); viviazhouyy@163.com (W.Z.)

**Abstract:** The ablation impulse of typical asteroid simulants irradiated by a nanosecond pulsed laser has been investigated in a vacuum environment. A torsional pendulum measurement system was constructed to calculate the impulse of laser ablation. A 10 ns pulsed laser was used, with a 1064 nm wavelength, a 900 mJ maximum pulse energy, and a millimeter-scale ablation spot diameter. Impulsive coupling characteristics of six typical targets that imitate the substance of asteroids with various laser fluences were analyzed. Furthermore, the impulse coupling coefficient curves of different materials were fitted. The results reveal that the minimum laser fluence corresponding to a measurable ablation impulse is approximately 2.5 J/cm<sup>2</sup>, and the optimum laser fluence corresponding to the maximum impulse coupling coefficient is approximately 14.0 J/cm<sup>2</sup>. The trends of the laser ablation impulse coupling curves are roughly consistent for the six materials. Impulse coupling characteristics of the six typical materials can be represented by the same polynomial within a 95% confidence interval, so a unified rule has been given. In actual deflection tasks of asteroids, the unified impulse coupling characteristic can be used to implement laser deflection techniques, especially when the material of the asteroid cannot be accurately judged in time.

**Keywords:** laser propulsion; laser ablation; impulse coupling coefficient; asteroid simulants; torsional pendulum system



**Citation:** Ma, Y.; Chang, H.; Zhou, W.; Jian, Z. Experimental Investigation of Impulsive Coupling Characteristics of Asteroid Simulants Based on Laser Ablation Propulsion. *Aerospace* **2024**, *11*, 388. <https://doi.org/10.3390/aerospace11050388>

Academic Editor: John Sinko

Received: 28 March 2024

Revised: 7 May 2024

Accepted: 9 May 2024

Published: 13 May 2024



**Copyright:** © 2024 by the authors. Licensee MDPI, Basel, Switzerland. This article is an open access article distributed under the terms and conditions of the Creative Commons Attribution (CC BY) license (<https://creativecommons.org/licenses/by/4.0/>).

## 1. Introduction

Scientifically, there are more than 11,000 asteroids active in near-Earth space, of which more than 2000 are considered to be “potentially hazardous” for impacting Earth [1]. The hazard of an asteroid impacting Earth is serious; for example, if a stone asteroid with a diameter of about 2 km collided with Earth, the explosion would release energy of up to about 1 trillion tons of TNT. In addition to the direct destruction of 1 million square kilometers of the area, a large number of sub-micron dust would be thrown into the stratosphere. The climate, ecology, and environment would experience a drastic catastrophe, thus resulting in a global effect [2–4].

To avoid asteroids impacting Earth, scientists have developed methods to predict asteroid orbits [5,6] and are committed to exploring efficient and feasible active defense means, including but not limited to the following: kinetic impactors with or without explosives [7,8]; altering the albedo of the asteroid surface [9]; direct thrust method [10,11]; laser ablation technology [12,13]; etc. Compared with other methods, laser deflection technology is not only reliable, but also can provide alterable continuous thrust to accurately control asteroids. The basic principle of laser deflection technology is shown in Figure 1. A laser platform with sufficiently high power irradiates the surface of an asteroid. The surface material of the asteroid ejects to produce the reaction force, which causes changes in the velocity of the asteroid. This will alter the spin state and orbit of the asteroid, thus preventing it from impacting Earth [14].

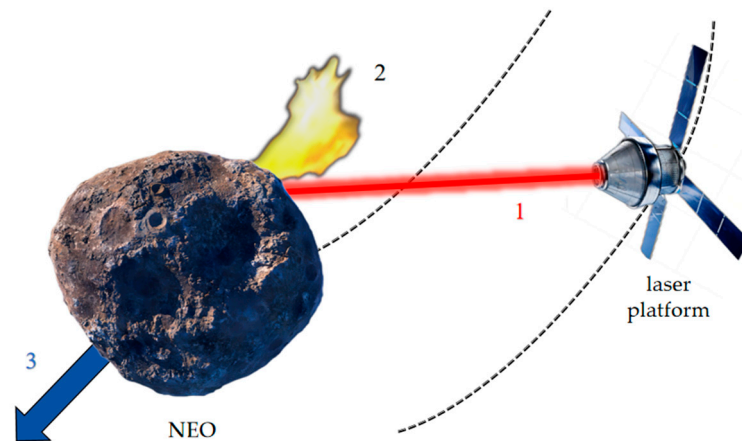


**Figure 1.** Schematic diagram of laser ablation deflection technology. (1) A high-power laser beam emitted by the laser platform; (2) ejecta plume of the surface material of the asteroid; (3) reaction force generated by the ejecta plume.

Related investigations have been conducted on laser ablation of asteroids. Gilkes et al. discussed the feasibility of a kW-class focused laser de-spinning asteroid and obtained empirical formulas to calculate the de-spinning time [15]. They found that laser ablation can not only stop the rotation quickly, but even reverse the direction of rotation. Walsh et al. conducted orbital analog simulations for laser arrays deflecting asteroids [16]. Simulation results concluded that the deflection effect has a strong dependence on the ablation time. Especially for ground-based laser systems, a short deflection time is almost invalid due to the duration of irradiation to the asteroid. Thiry et al. presented a new 3D thermal model of the laser ablation applied to the deflection of an asteroid, in order to calculate the efficiency of a laser deflection system [17]. They calculated that the coupling efficiency of a high-energy laser can reach  $80 \mu\text{N} \cdot \text{s}/\text{J}$  theoretically. Though the conversion efficiency of energy to laser power was neglected, the energy utilization rate of laser ablation technology was still considerable. In a word, the laser deflection technique is theoretically realizable. Although some results have been obtained in the area of laser deflection of asteroids, it is still a relatively open field. To the best of our knowledge, few experiments have been carried out on the laser ablation impulse effects of asteroids. The mechanical impulse data are still absent in the literature, especially for stone asteroids and carbonaceous asteroids.

In order to investigate the mechanical coupling efficiency of laser ablation of targets, the impulse coupling coefficient  $C_m$  is introduced. The  $C_m$  of the laser is the ratio of the laser ablation impulse to the incident laser energy, which reflects the conversion efficiency of the laser energy into an impulse. During the laser deflection of an asteroid, the propellant (the asteroid itself) can be considered limitless. Therefore, a larger  $C_m$  should be pursued. For pulsed laser ablation, the  $C_m$  is dependent on the laser fluence, the laser wavelength, the laser pulse duration, and the characteristics of materials [18]. The  $C_m$  shows the laser energy utilization rate more intuitively, which is very important for the selection of the laser parameters. Therefore, the investigation of the impulse coupling characteristics of asteroid materials is instructive for space propulsion [19], space debris removal [20], and other fields. In these applications, the pulsed laser, for example, the nanosecond pulsed laser, is widely selected as the irradiation source because of its higher impulse coupling [21]. In addition, the existence of laser facilities, like the National Ignition Facility (NIF) and the Laser Mégajoule (LMJ), indicates that kJ-pulses at a wavelength around  $10^3 \text{ nm}$  are generally applied [22,23]. These facilities operate on a nanosecond base and emit an extremely high pulse energy, which gives a foundation for laser asteroid deflection in the future.

Significant research has been conducted in the field of laser ablation propulsion. Sinko et al. developed a model for a  $\text{CO}_2$  laser that irradiates polyoxymethylene and similar polymers. Using this model, they introduced several main influencing factors of the  $C_m$ : laser wavelength, pulse duration, fluence, and material characteristics [24]. With increasing

laser fluence, they found the resolvable transition effects from the onset of vaporization to plasma. In 2013, Chang et al. established an approximate calculation model for the  $C_m$  of laser ablating space debris [25]. They introduced the ionization degree parameter and calculated that the optimal impulse coupling corresponded to an ionization degree of about 77%. It was indicated that the optimal impulse coupling is reached when the plasma is dominant. In 2020, Yu et al. experimentally obtained the impulse coupling mechanism of the aluminum target [26]. The results showed that the optimal  $C_m$  of  $21.04 \mu\text{N} \cdot \text{s}/\text{J}$  corresponded to the laser fluence of  $15.92 \text{ J}/\text{cm}^2$ . The influence of the plasma shielding effect on the  $C_m$  was further verified by deducing the relative energy coupling efficiency from the plume front positions. Besides experimental investigations, some physical models for laser ablation impulse and  $C_m$  have been generally discussed. Phipps et al. established the photochemical model [27] and the photothermal model was deduced by Carlslaw and Jaeger [28]. Sinko et al. compared the above-mentioned physical models of laser ablation impulse generation [29]. For practical deflection missions, the mechanical response plays a crucial role in determining the size and the power of the laser array. Furthermore, measuring the impulse of a single laser pulse is challenging, because the system must be accurate enough to detect tiny transient responses. The torsional pendulum system is an ideal tool used in laser ablation. High accuracy and high stability make it more suitable to measure the impulse of a single laser pulse [30,31].

This paper aims to determine the impulse coupling characteristics of nanosecond pulsed lasers ablating typical asteroid simulants. An experimental system for nanosecond pulsed laser ablation of typical asteroid simulants in a vacuum environment was constructed. A torsion pendulum system was built to measure the mechanical effects of laser ablation. The optimal impulse coupling of various types of asteroid simulants was measured. In the end, a universal rule of the nanosecond pulsed laser ablation of asteroid simulants was summarized.

## 2. Experimental Set-Up

The schematic diagram of the experimental system is shown in Figure 2. The whole experiment was carried out in a vacuum chamber with a vacuum degree of  $10^{-3}$  Pa. A laser with  $\lambda = 1064 \text{ nm}$  and  $\tau = 10 \text{ ns}$  was emitted by a Q-switched Nd:YAG laser with a maximum pulse energy of 900 mJ. The laser was focused by an optical lens and then ablated the asteroid material with an adjustable ablation spot radius. The light intensity distribution was roughly Gaussian. A torsion pendulum system was constructed to measure the impulse produced by single-pulse laser ablation. A two-dimensional displacement platform was installed underneath the torsion pendulum system. A displacement sensor (10 mm range, 100 nm resolution) was installed at the end of the torsional pendulum beam. It was sensitive enough to detect the tiny displacements produced by single-pulse laser ablation.

Six kinds of typical materials that imitate the substance of asteroids were selected as ablation targets for this investigation [32]: basalt, iron meteorite, Altay iron meteorite, Shid-ian meteorite, ordinary chondrite, and carbonaceous chondrite. The physical, mechanical, and thermal physical properties of the six asteroid simulants are presented in Table 1. As a reference material, carbonaceous chondrite was compared with the other five types of stone asteroid simulants. When the pulsed laser ablated the surface of asteroid simulants, the surface irradiation zone was quickly heated to melt and boil, as well as forming the target vapor. The target vapor was further electrolyzed to form plasma plumes. Subsequently, the torsion pendulum beam began to oscillate. The displacement sensor was used to measure the maximum torsion angle of the beam, so as to calculate the impulse generated by the laser ablation.

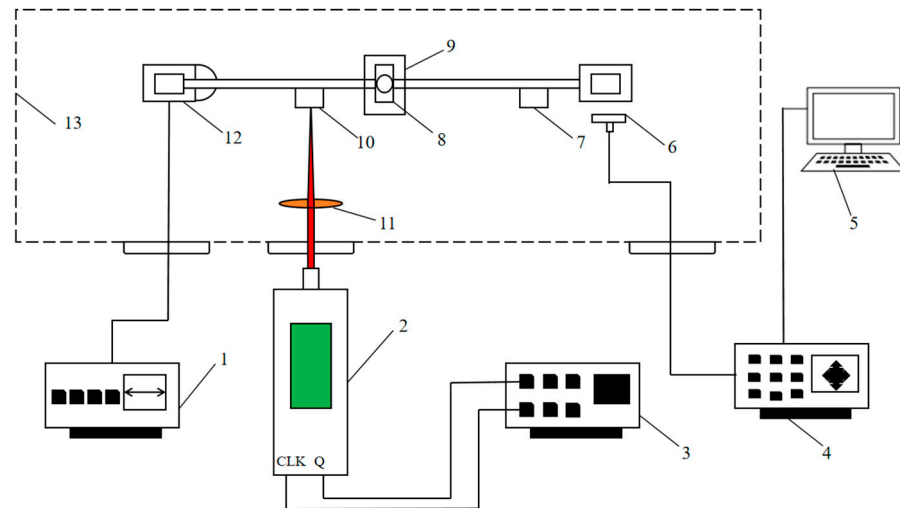


**Figure 2.** Schematic diagram of the experimental system. (1) Programmable power supply; (2) the Q-switched Nd:YAG laser; (3) digital pulse generator; (4) data acquisition unit; (5) computer; (6) displacement sensor; (7) counterweight block; (8) pivot; (9) two-dimensional displacement platform; (10) target material; (11) optical lens; (12) damper; (13) vacuum chamber.

**Table 1.** The characteristic parameters of the six asteroid simulants.

Sample	$\rho$ (g/cm <sup>3</sup> )	$\sigma_{bc}$ (MPa)	$\phi$ (%)	$c$ (J/kg·K)	$\lambda$ (W/m·K)
Basalt	3.60	211.5	2.9	682 ± 35	3.5 ± 0.18
Iron meteorite	8.12	398.0	1.2	480 ± 25	51.0 ± 2.55
Altay iron meteorite	8.17	375.0	2.3	548 ± 28	63.0 ± 3.15
Carbonaceous chondrite	3.11	45.3	22.8	871 ± 44	1.9 ± 0.09
Schieden meteorite	2.3	66.1	20.1	909 ± 45	1.5 ± 0.08
Ordinary chondrite	3.39	143.3	1.9	707 ± 35	2.7 ± 0.14

### 3. Method of Laser Ablation Impulse Measurement

The torsion pendulum system is an ideal device to measure the micro pulsed laser ablation impulse because of the following features. Firstly, the torsional pendulum vibration equation is relatively simple. As a second-order differential equation, it has a single vibrational frequency and period. The system parameters can be easily calibrated, making it convenient to analyze and evaluate the impulse induced by laser ablation. Secondly, the torsional vibration is in the horizontal plane of the parallel base; therefore, it is insensitive to vibration interference in the direction perpendicular to the base. The second-order vibration equation of the typical torsional pendulum can be simplified as follows [33]:

$$\ddot{\theta} + 2\zeta\omega_n\dot{\theta} + \omega_n^2\theta = \frac{f(t)L}{J} \quad (1)$$

where  $\theta$  is the torsion angle,  $\omega_n$  is the natural frequency,  $J$  is the rotational inertia of the torsional pendulum system, and  $\zeta$  is the damping ratio, with  $f(t)$  and  $L$  being the thrust and the actuating arm, respectively. The ablation time of the single-pulse laser is so short that it can be regarded as an instantaneous action. Therefore, the torsional pendulum vibration equation can be represented as follows:

$$\begin{cases} \ddot{\theta} + 2\zeta\omega_n\dot{\theta} + \omega_n^2\theta = 0 & t \geq 0 \\ \theta(t=0) = 0, \dot{\theta}(t=0) = \dot{\theta}_0 \end{cases} \quad (2)$$

Solving Equation (2) with the initial torsion angle  $\theta_0$  and angular velocity  $\dot{\theta}_0$  obtains [14]:

$$\theta(t) = \frac{\dot{\theta}_0}{\omega_d} e^{-\zeta\omega_n t} \sin \omega_d t \quad (3)$$

$$\dot{\theta}(t) = \frac{\dot{\theta}_0}{\omega_d} e^{-\zeta\omega_n t} (-\zeta\omega_n \sin \omega_d t + \omega_d \cos \omega_d t) \quad (4)$$

The time  $t_{\max}$  corresponding to the maximum torsion angle of the beam can be expressed as follows:

$$t_{\max} = \frac{1}{\omega_d} \arctan \frac{\sqrt{1-\zeta^2}}{\zeta} \quad (5)$$

From Equations (3) and (5), we can calculate the maximum torsion angle  $\theta_{\max}$ :

$$\theta_{\max} = \dot{\theta}_0 \frac{e^{-\frac{\zeta}{\sqrt{1-\zeta^2}} \arctan \frac{\sqrt{1-\zeta^2}}{\zeta}}}{\omega_n} \quad (6)$$

According to the theorem of moment of momentum:

$$I \cdot D = J\dot{\theta}_0 \quad (7)$$

where  $I$  is the laser ablation impulse. Substituting Equation (7) into Equation (6) obtains the relationship between the impulse and the maximum torsion angle of the torsion beam:

$$I = \frac{J\omega_n}{L} \exp\left(\frac{\zeta}{\sqrt{1-\zeta^2}} \arctan \frac{\sqrt{1-\zeta^2}}{\zeta}\right) \theta_{\max} \quad (8)$$

The torsion angle caused by the micro-impulse meets the small angle condition:

$$\theta_{\max} \approx \sin \theta_{\max} \approx \frac{d_{\max}}{L_m} \quad (9)$$

where  $L_m$  is the measuring arm. Therefore, the impulse can be represented by the maximum displacement measured by the displacement sensor:

$$I = \frac{J\omega_n}{LL_m} \exp\left(\frac{\zeta}{\sqrt{1-\zeta^2}} \arctan \frac{\sqrt{1-\zeta^2}}{\zeta}\right) d_{\max} \quad (10)$$

Obviously, in Equation (10), except for the measured parameter  $d_{\max}$ , all other parameters are system parameters which must be calibrated before the impulse test. The results and errors of the calibration are shown in Table 2 [34].

**Table 2.** Results and errors of torsional pendulum system calibration.

Parameter	Result	Standard Deviation
Actuating arm $L$ (mm)	100	0.52
Measuring arm $L_m$ (mm)	150	0.46
Natural frequency $\omega_n$ (rad/s)	4.83632	0.06004
Rotational inertia $J$ (kg·m <sup>2</sup> )	$4.06753 \times 10^{-4}$	$9.0235 \times 10^{-6}$
Damping ratio $\zeta$	$9.15984 \times 10^{-5}$	$2.9854 \times 10^{-5}$

## 4. Results and Discussion

### 4.1. Impulse Coupling Characteristics of Asteroid Simulants

Prior to the experiment, the samples were first cut into 4 mm thick pieces, with a length and width of 10 mm. Before placing the targets into the vacuum chamber, the

surfaces to be irradiated were ground and polished. It should be pointed out that the surface of asteroids is always rough and dusty in the real space environment, which may have effects on the laser ablation impulse characteristics. However, in our experiment, the surface influences of the asteroid material were not taken into account because of the complicated surface information of the real asteroid materials, but it is important for this to be considered in future research. Figure 3 presents the ablation spots of six typical asteroid simulants irradiated by the nanosecond pulsed laser. The laser energy was obtained accurately after calibration, and the spot area was measured by the beam quality analyzer. During the experiment, the laser energy was gradually increased. The range of the ablation laser fluence was  $2.15\sim 25.23\text{ J/cm}^2$ , corresponding to a power density of  $2.15 \times 10^8\sim 2.52 \times 10^9\text{ W/cm}^2$ . The laser fluence we selected covered the vaporization phase and the ionization phase. Five groups of repeated experiments were performed for each laser fluence to reduce experimental errors. According to the above Equation (10), the average value and error of the impulses and the impulse coupling coefficients of six asteroid simulants were calculated.

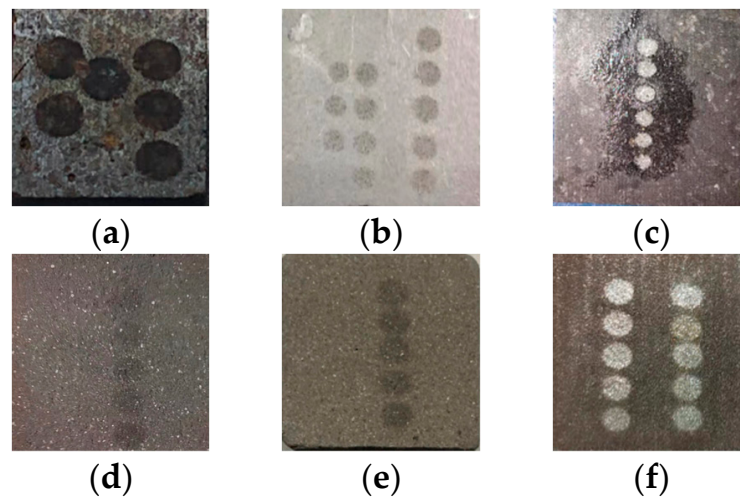


**Figure 3.** Ablation spots of six types of asteroid simulants: (a) carbonaceous chondrite; (b) iron meteorite; (c) basalt; (d) Shidian meteorite; (e) ordinary chondrite; (f) Altay iron meteorite.

The relationship between laser fluence and the impulse of the six types of asteroid simulants is shown in Figure 4. It can be seen that the impulse of the six materials increases linearly with the growth of the laser fluence. Compared with other stone asteroid simulants, the carbonaceous chondrite obtains the highest impulse at the same laser fluence. This means that the carbonaceous chondrite can absorb more laser energy for the same laser fluence, resulting in a larger impulse. The energy coupling efficiency of other stone materials is comparatively lower. This is likely because the carbonaceous chondrite, which is composed of loosely bound powders, is a volume absorber. Therefore, the same energy can remove more material from the surface of volume absorbers, correspondingly causing a higher impulse [18]. For stone asteroid simulants, the Shidian meteorite obtains the lowest impulse, and the impulse disparity grows with increasing laser fluence. When the laser fluence is less than  $10\text{ J/cm}^2$ , the maximum impulse disparity between different materials is below  $5\text{ }\mu\text{N}\cdot\text{s}$ . However, when the laser fluence reaches  $20\text{ J/cm}^2$  or more, the disparity is more than  $15\text{ }\mu\text{N}\cdot\text{s}$ .

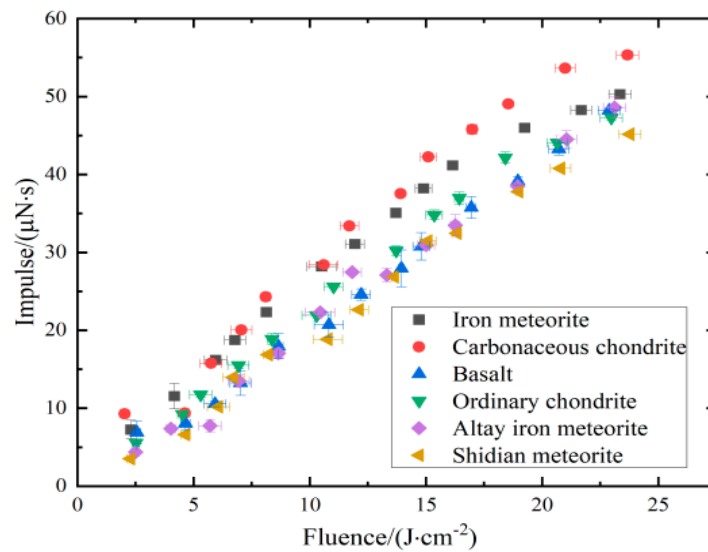


**Figure 4.** Impulse of six types of asteroid simulants irradiated by different laser fluences (the beam size was approximately  $500 \mu\text{m}$  at  $1/e^2$ , and the laser pulse duration was 10 ns).

Figure 5 presents the impulse coupling coefficient of the six asteroid simulants depending on the pulsed laser fluence. It can be seen that the variation trend of the impulse coupling coefficients for different asteroid materials is roughly consistent. It shows an overall trend of increasing rapidly to the maximum, and then decreasing slowly. A measurable minimum impulse corresponds to a laser fluence of  $2.5 \text{ J/cm}^2$ . With the laser fluence increasing, the  $C_m$  reaches a peak value when the laser fluence is  $14.0 \text{ J/cm}^2$ . Based on a previous experimental analysis, it was shown that the position of the maximum  $C_m$  was close to the plasma production threshold in a broad range of radiation wavelength and pulse duration [35]. Furthermore, a rising trend in  $C_m$  from vapor formation is compensated by a declining trend due to the increased laser energy required for accelerating plasma. In this fluence, the conversion of laser energy into an impulse is the most efficient. Therefore, the energy density corresponding to the maximum impulse coupling coefficient is usually called the optimal laser fluence. As seen in some studies, the optimal value of the  $C_m$  has been repeatedly observed for metals and polymer materials [26,35–37].

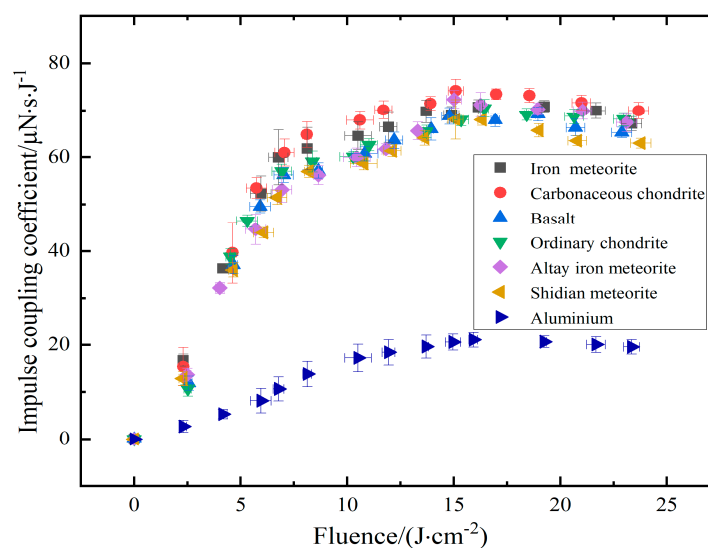


**Figure 5.** Impulse coupling coefficient of six types of asteroid simulants and the aluminum irradiated by different laser fluences (the beam size was approximately  $500 \mu\text{m}$  at  $1/e^2$ , and the laser pulse duration was 10 ns).

As shown in Figure 5, the  $C_m$  grows rapidly with increasing laser fluence when the laser fluence is lower than the optimum value. Nevertheless, the  $C_m$  decreases obviously after the laser fluence exceeds the optimum value. One possible reason is that the plasma phase begins to appear as the laser fluence increases. With more laser energy deposited onto the surface of the material, the vapor produced by melting and evaporating will be ionized into the plasma plume [24]. Due to the inverse bremsstrahlung effect, part of the incident laser energy is absorbed by the plasma plume, resulting in a decrease in the absorptivity of the laser [38]. In a word, during the vapor phase, the growth of the laser fluence increases the evaporation rate to produce a higher impulse. However, with the further growth of laser fluence, the impulse coupling coefficient decreases due to the plasma shielding effect. In our previous studies, it was shown that the impulse coupling coefficients of metallic materials have the same characteristics [26]. As shown in Figure 5, it is noteworthy that for the asteroid simulants used in our experiment, their optimal ablation laser fluence is comparable to the metal aluminum. However, their maximum impulse coupling coefficients are several times larger than the metal aluminum, which means a higher efficiency.

#### 4.2. Unified Impulsive Coupling Characteristic of Multi-Materials

The disparity between the  $C_m$  of the six types of asteroid simulants is relatively small. Thus, the curves have approximate fitting parameters and a unified variation trend with the growth of the laser fluence, as shown in Table 3 and Figure 6. To further investigate the universal rule of the impulse coupling characteristics of multiple materials, a polynomial fitting of the  $C_m$  of the six types of asteroid simulants was performed. The fitting curve is shown in Figure 7. It is obvious that the change characteristic of the unified fitting curve is approximately consistent with one single material curve in Figure 6. Quartic polynomial fitting indicated that the  $R^2$  of the unified fitting curve reached 0.9318, and the RMSE of the unified fitting curve was only 1.9596. The confidence level for both the confidence band and the prediction band was above 95%. The fitting function of single asteroid simulants and the unified fitting curve are shown in Equation (11) and Table 3, where  $\phi_0$  is the laser fluence. Therefore, it is reasonable to consider that the impulsive coupling rule of these six typical asteroid materials can be represented by a unified fitting curve. In actual deflection tasks of asteroids, the unified impulse coupling characteristic can be used to implement laser deflection techniques, especially when the material of the asteroid cannot be accurately judged in time.

$$f(x) = C_m(\phi_0) = \sum_{i=0}^4 A_i \phi_0^i \quad (11)$$

**Table 3.** Fitting parameters of single materials and the unified fitting curve.

Fitting Curve	$A_0$	$A_1$	$A_2$	$A_3$	$A_4$
Basalt	$-4.49474 \times 10^{-5}$	8.99946	-0.17181	-0.01589	$5.11478 \times 10^{-4}$
Iron meteorite	$4.50431 \times 10^{-6}$	9.91379	-0.34793	-0.00322	$2.26521 \times 10^{-4}$
Carbonaceous chondrite	$-6.17184 \times 10^{-5}$	13.3436	-0.89132	0.2634	$-3.05104 \times 10^{-4}$
Ordinary chondrite	$4.47812 \times 10^{-6}$	10.43798	-0.47363	0.00311	$1.48136 \times 10^{-4}$
Altay iron meteorite	$-4.22016 \times 10^{-5}$	8.45032	-0.23354	-0.00394	$1.61539 \times 10^{-4}$
Shidian meteorite	$4.54965 \times 10^{-6}$	9.00695	-0.26015	-0.00777	$3.13997 \times 10^{-4}$
Unified fitting curve	-23.95029	18.70541	-1.38109	0.04228	$-4.65438 \times 10^{-4}$

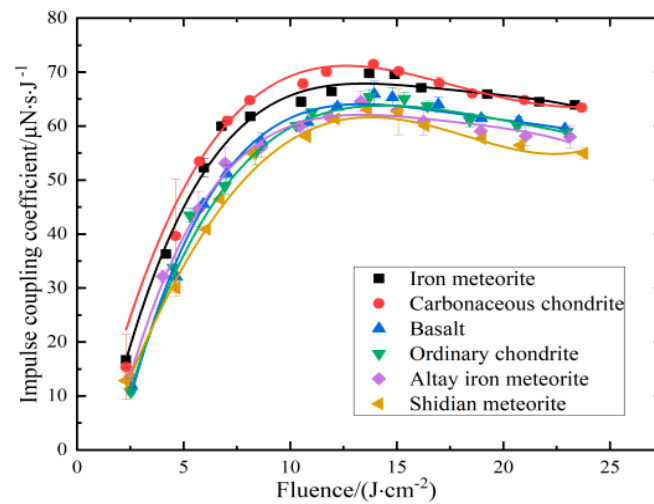


**Figure 6.** Comparison of impulse coupling curves of six types of asteroid simulants (the beam size was approximately  $500\ \mu\text{m}$  at  $1/e^2$ , and the laser pulse duration was 10 ns).

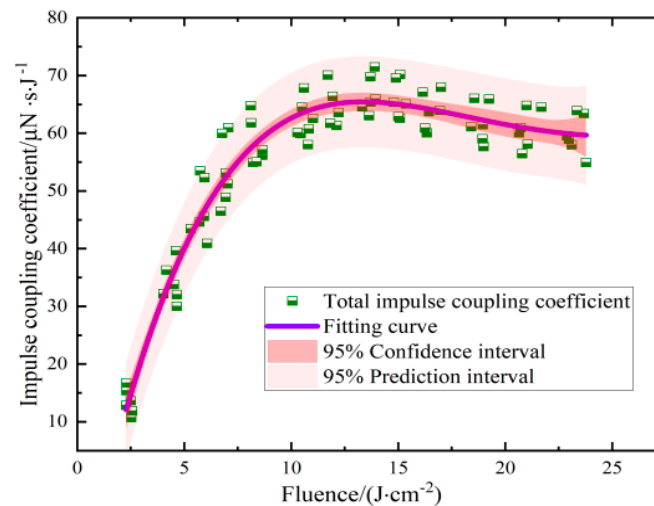


**Figure 7.** Fitting curves for the impulsive coupling characteristics of six types of asteroid simulants (the beam size was approximately  $500\ \mu\text{m}$  at  $1/e^2$ , and the laser pulse duration was 10 ns).

## 5. Conclusions

In this paper, the impulse coupling characteristics of asteroid simulants irradiated by nanosecond pulsed laser light were investigated. A torsion pendulum system was used to measure the single-pulse laser ablation impulse, and thus determined the optimal laser fluence corresponding to the peak of the impulse coupling coefficient. The results show that the carbonaceous chondritic obtains the largest impulse with the same laser fluence, slightly higher than the other five kinds of stone asteroid simulants. The impulse obtained by the Shidian meteorite is the smallest, and the gap between the Shidian meteorite and the carbonaceous chondritic grows larger as the laser fluence increases. Furthermore, the  $C_m$  of six kinds of asteroid simulants were analyzed in comparison. The variation trends of the  $C_m$  for the six different asteroid simulants are generally consistent. By means of the fourth-order polynomial fitting, both the confidence band and the prediction band are above 95%. Therefore, a unified fitting curve is reliable to express the universal rules of the  $C_m$  for the six different kinds of asteroid simulants.

According to the experimental data, a measurable impulse appeared in the torsional pendulum system when the laser fluence was  $2.5\ \text{J}/\text{cm}^2$ . As the laser fluence reached  $14.0\ \text{J}/\text{cm}^2$ , the  $C_m$  reached its peak. At this fluence, the laser energy efficiency was at a maximum, and the most ideal ablation effect had been achieved. During the period

of laser fluence at less than  $14.0 \text{ J/cm}^2$ , the  $C_m$  gradually increased with the increment in laser fluence. This is because the larger the laser fluence, the higher the rate of vapor ejection, which produced a greater recoil impulse. When the laser fluence was larger than  $14.0 \text{ J/cm}^2$ , the  $C_m$  began to decrease slowly with the increase in laser fluence. This is due to the appearance of the plasma phase, and the plasma shielding effect became stronger as the laser fluence increased. In a practical deflection mission, the asteroid itself acts as the propellant to meet the small impulse, long time deflection. Therefore, from an energy saving point of view, a higher impulse coupling coefficient should be pursued as much as possible. Furthermore, in the actual deflection mission planning, orbital simulation is necessary to determine the appropriate laser parameters, including but not limited to laser fluence, laser irradiation duration, and laser ablation area. Based on the impulse coupling characteristics presented in this investigation, orbital simulations should be further carried out in future research to complete the asteroid deflection mission analysis process.

**Author Contributions:** Conceptualization, H.C. and W.Z.; methodology, Y.M., H.C. and Z.J.; validation, H.C. and W.Z.; formal analysis, Y.M.; investigation, Y.M. and Z.J.; resources, H.C. and W.Z.; data curation, Y.M. and Z.J.; writing—original draft preparation, Y.M. and Z.J.; writing—review and editing, H.C. and W.Z.; visualization, Z.J.; funding acquisition, H.C. and W.Z. All authors have read and agreed to the published version of the manuscript.

**Funding:** This research was funded by the National Natural Science Foundation of China under Grant 11602304 and Grant 11502301.

**Data Availability Statement:** The data presented in this study are available on request from the corresponding author. The data are not publicly available due to privacy.

**Acknowledgments:** The authors would like to acknowledge Chenghao Yu and Gang Ji for their assistance with the experiments.

**Conflicts of Interest:** The authors declare no conflicts of interest.

## Nomenclature

TNT	Trinitrotoluene
NEO	Near-Earth Objects
NIF	National Ignition Facility
LMJ	Laser Mégajoule
RMSE	Root Mean Square Error
$R^2$	Goodness of Fit
$\rho$	Bulk density ( $\text{g/m}^3$ )
$\sigma_{bc}$	Compressive strength (MPa)
$\varphi$	Porosity (%)
$c$	Specific heat capacity ( $\text{J/kg}\cdot\text{K}$ )
$\lambda$	Thermal conductivity ( $\text{W/m}\cdot\text{K}$ )
$C_m$	Impulse coupling coefficient ( $\text{N}\cdot\text{s/J}$ )
$\theta$	Torsion angle of the torsion pendulum (rad)
$\theta_0$	Initial torsion angle (rad)
$\theta_{\max}$	Maximum torsion angle (rad)
$t_{\max}$	Time corresponding to maximum torsion angle (s)
$\zeta$	Damping ratio
$\omega_n$	Natural frequency (rad/s)
$J$	Rotational inertia ( $\text{kg}\cdot\text{m}^2$ )
$f(t)$	Thrust (N)
$L$	Actuating arm (mm)
$L_m$	Measure arm (mm)
$D$	Arm of the impulse force (mm)
$d_{\max}$	Maximum displacement of the torsion pendulum (mm)
$\phi_0$	Laser fluence ( $\text{J/cm}^2$ )

## References

1. Chapman, C.R. The hazard of near-Earth asteroid impacts on earth. *Earth Planet. Sci. Lett.* **2004**, *222*, 1–15. [CrossRef]
2. Campbell, J.W.; Phipps, C.; Smalley, L.; Reilly, J.; Boccio, D. The Impact Imperative: Laser Ablation for Deflecting Asteroids, Meteoroids, and Comets from Impacting the Earth. *AIP Conf. Proc.* **2003**, *664*, 509–522.
3. Chesley, S.R.; Ward, S.N. A Quantitative Assessment of the Human and Economic Hazard from Impact-generated Tsunami. *Nat. Hazards* **2006**, *38*, 355–374. [CrossRef]
4. Saito, T.; Kaiho, K.; Abe, A.; Katayama, M.; Takayama, K. Numerical simulations of hypervelocity impact of asteroid/comet on the earth. *Int. J. Impact Eng.* **2006**, *33*, 713–722. [CrossRef]
5. Shao, M.; Nemati, B.; Zhai, C.; Turyshev, S.G.; Sandhu, J.; Hallinan, G.; Harding, L.K. Finding Very Small Near-Earth Asteroids using Synthetic Tracking. *Astrophys. J.* **2013**, *782*, 1–7. [CrossRef]
6. Desmars, J.; Bancelin, D.; Hestroffer, D.; Thuillot, W. Statistical and numerical study of asteroid orbital uncertainty. *Astron. Astrophys.* **2013**, *554*, 393–403. [CrossRef]
7. McInnes, C.R. Deflection of near-Earth asteroids by kinetic energy impacts from retrograde orbits. *Planet. Space Sci.* **2004**, *52*, 587–590. [CrossRef]
8. Koenig, J.D.; Chyba, C.F. Impact Deflection of Potentially Hazardous Asteroids Using Current Launch Vehicles. *Sci. Glob. Secur.* **2007**, *15*, 57–83. [CrossRef]
9. Vasile, M.; Maddock, C.A. On the deflection of asteroids with mirrors. *Celest. Mech. Dyn. Astr.* **2010**, *107*, 265–284. [CrossRef]
10. Walker, R.; Izzo, D.; Negueruela, C.D.; Summerer, L.; Ayre, M.; Vasile, M. Concepts for Near Earth Asteroid Deflection using Spacecraft with Advanced Nuclear and Solar Electric Propulsion Systems. *J. Br. Interplanet. Soc.* **2005**, *59*, 268–278.
11. Colombo, C.; Vasile, M.; Radice, G. Semi-Analytical Solution for the Optimal Low-Thrust Deflection of Near-Earth Objects. *J. Guid. Control Dyn.* **2009**, *32*, 796–809. [CrossRef]
12. Vetrivano, M.; Colombo, C.; Vasile, M. Asteroid rotation and orbit control via laser ablation. *Adv. Space Res.* **2016**, *57*, 1762–1782. [CrossRef]
13. Gibbings, A.; Vasile, M.; Watson, I.; Hopkins, J.-M.; Burns, D. Experimental analysis of laser ablated plumes for asteroid deflection and exploitation. *Acta Astronaut.* **2013**, *90*, 85–97. [CrossRef]
14. Zhou, W.; Chang, H.; Ye, J.; Li, N. Impulse of planar and sphere target by nanosecond laser ablation in a large beam spot. *Laser Phys.* **2020**, *30*, 066002. [CrossRef]
15. Gilkes, A.; Brashears, T.; Lubin, P. De-Spinning Asteroids: Using Laser Ablation to Manipulate Asteroid Motion. Internal UC Santa Barbara Poster. 2015. Available online: <https://www.deepspace.ucsb.edu/wp-content/uploads/2013/09/Aidan-Gilkes-RMP-Paper-Final-correct-fig-4.pdf> (accessed on 5 May 2024).
16. Zhang, Q.; Walsh, K.J.; Melis, C.; Hughes, G.B.; Lubin, P.M. Orbital Simulations on Deflecting Near-Earth Objects by Directed Energy. *Publ. Astron. Soc. Pac.* **2016**, *128*, 045001. [CrossRef]
17. Thiry, N.; Vasile, M. Recent Advances in Laser Ablation Modelling for Asteroid Deflection Methods. In Proceedings of the SPIE Optical Engineering+ Applications, San Diego, CA, USA, 17 September 2014.
18. Phipps, C.R.; Birkan, M.; Bohn, W.; Eckel, H.A.; Horisawa, H.; Lippert, T.; Michaelis, M.; Rezunkov, Y.; Sasoh, A.; Schall, W.; et al. Review: Laser-Ablation Propulsion. *J. Propul. Power* **2010**, *26*, 609–637. [CrossRef]
19. Bergstue, G.; Fork, R.; Reardon, P. An advanced optical system for laser ablation propulsion in space. *Acta Astronaut.* **2014**, *96*, 97–105. [CrossRef]
20. Shen, S.; Jin, X.; Chang, H. Cleaning space debris with a space-based laser system. *Chin. J. Aeronaut.* **2014**, *27*, 805–811. [CrossRef]
21. Bhargava, P.; Kumar, M.; Kumar, H.; Pandit, P.; Pandey, R.; Nath, A.K. Impulse coupling in laser-driven microtargets. *Pramana* **2004**, *62*, 923–932. [CrossRef]
22. Haynam, C.; Wegner, P.; Auerbach, J.; Bowers, M.; Dixit, S.; Erbert, G.; Heestand, G.; Hennesian, M.; Hermann, M.; Jancaitis, K.; et al. National Ignition Facility laser performance status. *Appl. Opt.* **2007**, *46*, 3276–3303. [CrossRef]
23. CEA—Direction des Applications Militaires. Laser Megajoule: Description de l’Installation LMJ. 2023. Available online: <https://www-lmj.cea.fr/lmj-description.html> (accessed on 6 May 2024).
24. Sinko, J.E.; Phipps, C.R. Modeling CO<sub>2</sub> laser ablation impulse of polymers in vapor and plasma regimes. *Appl. Phys. Lett.* **2009**, *95*, 131105. [CrossRef]
25. Chang, H.; Jin, X.; Wen, M. Analytical Model for Calculating Laser Ablation Impulse Coupling Coefficient. *High Power Laser Part. Beams* **2013**, *25*, 1110–1114. [CrossRef]
26. Yu, C.; Zhou, W.; Chang, H.; Chen, Y. Experimental Research on Impulse Coupling Characteristics and Plasma Plume Dynamics of a Nanosecond Pulsed Laser Irradiated Aluminum Target. *IEEE Access* **2020**, *8*, 205272–205281. [CrossRef]
27. Phipps, C.R.; Harrison, R.F.; Shimada, T.; York, G.W.; Turner, T.P.; Corlis, X.F.; Steele, H.S.; Haynes, L.C. Enhanced vacuum laser-impulse coupling by volume absorption at infrared wavelengths. *Laser Part. Beams* **1990**, *8*, 281–298. [CrossRef]
28. Carslaw, H.S.; Jaeger, J.C. Conduction of heat in solids. *Math. Gaz.* **1959**, *1*, 75. [CrossRef]
29. Sinko, J.E.; Gregory, D.A.; Phipps, C.; Komurasaki, K.; Sinko, J. Models for laser ablation mass removal and impulse generation in vacuum. *AIP Conf. Proc.* **2010**, *1230*, 193–203.
30. Phipps, C.R.; Luke, J.R. Diode Laser-Driven Microthrusters: A New Departure for Micropropulsion. *AIAA J.* **2002**, *40*, 310–318. [CrossRef]

31. Yang, Y.; Tu, L.; Yang, S.; Luo, J. A torsion balance for impulse and thrust measurements of micro-Newton thrusters. *Rev. Sci. Instrum.* **2012**, *83*, 015105. [[CrossRef](#)] [[PubMed](#)]
32. Wang, D.; Liu, J. *Introduction to Chinese Meteorites*, 1st ed.; Science Press: Beijing, China, 1993; pp. 17–61.
33. Wang, G.; Hong, Y. Modeling error analysis of micro-impulse measurements. *J. Propul. Technol.* **2009**, *30*, 509–512.
34. Zhou, W.; Hong, Y.; Chang, H. A microNewton thrust stand for average thrust measurement of pulsed microthruster. *Rev. Sci. Instrum.* **2013**, *84*, 125115. [[CrossRef](#)]
35. Phipps, C.R.; Boustie, M.; Chevalier, J.M.; Baton, S.; Brambrink, E.; Berthe, L.; Schneider, M.; Videau, L.; Boyer, S.A.E.; Scharring, S. Laser impulse coupling measurements at 400 fs and 80 ps using the LULI facility at 1057 nm wavelength. *J. Appl. Phys.* **2017**, *122*, 193103. [[CrossRef](#)]
36. Phipps, C.R.; Turner, T.P.; Harrison, R.F.; York, G.W.; Osborne, W.Z.; Anderson, G.K.; King, T.R. Impulse coupling to targets in vacuum by KrF, HF, and CO<sub>2</sub> single-pulse lasers. *J. Appl. Phys.* **1988**, *64*, 1083–1096. [[CrossRef](#)]
37. Burdonskii, I.N.; Leonov, A.G.; Makarov, K.N.; Yufa, V.N. Experimental investigation of laser ablation of stone polycrystalline targets. *Quantum Electron.* **2020**, *50*, 763. [[CrossRef](#)]
38. Bindhu, C.V.; Harilal, S.S.; Tillack, M.S.; Najmabadi, F.; Gaeris, A.C. Laser propagation and energy absorption by an argon spark. *J. Appl. Phys.* **2003**, *94*, 7402–7407. [[CrossRef](#)]

**Disclaimer/Publisher’s Note:** The statements, opinions and data contained in all publications are solely those of the individual author(s) and contributor(s) and not of MDPI and/or the editor(s). MDPI and/or the editor(s) disclaim responsibility for any injury to people or property resulting from any ideas, methods, instructions or products referred to in the content.